Astronomy & Astrophysics

Non-thermal emission in the core of Perseus: results from a long *XMM-Newton* observation

S. Molendi[1] and F. Gastaldello[2,3,4]

1   IASF-Milano, INAF, via Bassini 15, 20133 Milano, Italy
    e-mail: silvano@iasf-milano.inaf.it
2   Dip. di Astronomia, Università di Bologna, via Ranzani 1, 40127 Bologna, Italy
    e-mail: fabio.gastaldello@unibo.it
3   INAF, Osservatorio Astronomico di Bologna, via Ranzani 1, Bologna 40127, Italy
4   Department of Physics and Astronomy, University of California at Irvine, 4129 Frederick Reines Hall, Irvine,
    CA 92697-4575, USA

ABSTRACT

We employ a long *XMM-Newton* observation of the core of the Perseus cluster to validate claims of a non-thermal component discovered with *Chandra*. From a meticulous analysis of our dataset, which includes a detailed treatment of systematic errors, we find the 2–10 keV surface brightness of the non-thermal component to be less than about 5×10^{-16} erg cm^{-2} s^{-1} arcsec^{-2}. The most likely explanation for the discrepancy between the *XMM-Newton* and *Chandra* estimates is a problem in the effective area calibration of the latter. Our *EPIC*-based magnetic field lower limits do not disagree with Faraday rotation measure estimates on a few cool cores and with a minimum energy estimate on Perseus. In the not too distant future *Simbol-X* may allow detection of non-thermal components with intensities more than 10 times lower than those that can be measured with *EPIC*; nonetheless even the exquisite sensitivity within reach for *Simbol-X* might be insufficient to detect the IC emission from Perseus.

Key words. galaxies: clusters: general – galaxies: clusters: individual: Perseus – X-rays: galaxies: clusters

1. Introduction

Although the bulk of the energy radiated from clusters is of thermal nature, non-thermal mechanisms play an important role. Indeed the characterization of non-thermal components provides much needed clues to the physical process presiding over the formation and evolution of clusters. In some of the more disturbed objects, evidence of non-thermal processes has been known for quite some time. Radio observations indicate that merging clusters are often the site of cluster-wide synchrotron emission, the so called radio halos and radio relics (Cassano et al. 2007, and references therein). Radio data, polarimetric or not, has been used to provide estimates of magnetic fields in clusters. Unfortunately estimates based on Faraday rotation measures (hereafter RM) or minimum-energy arguments are affected by large uncertainties. In the case of RM estimates the unknown field topology (Enßlin & Vogt 2003) and the accessability of only a few, not necessarily representative, lines of sight (Rudnick & Blundell 2003), are a major source of concern, while for minimum energy arguments the proton to electron ratio, and the applicability of the argument itself play an equally critical role.

It has been recognized for quite some time that detection of inverse Compton (hereafter IC) emission at X-ray wavelengths can provide an alternative method to estimate cluster magnetic fields (Rephaeli et al. 1987). Detection and characterization of the so called hard tails is by no means a trivial task: the signal, if there is one, is caught between the hammer of the thermal emission and the anvil of the instrumental background. So far, only detections at a few sigma level have been reported (for a recent review see Rephaeli et al. 2008), and at least in one case, Coma (Fusco-Femiano et al. 1999, 2004, 2007), they have been challenged (Rossetti & Molendi 2004, 2007).

Aim of the present work is to employ a long *XMM-Newton* observation of the Perseus core to validate claims about a non-thermal emission component discovered with *Chandra* (Sanders et al. 2004, 2005; Sanders & Fabian 2007). The major advantage of the *XMM-Newton* observation is the better sensitivity at high energies (~6 keV) of the *EPIC* detectors with respect to the *ACIS-S3*; this is illustrated in Fig. 1 where we show the ratio of background to source intensity in a representative region, a ring with bounding radii 1′–2′ centered on the emission peak. The *Chandra* ratio rises very rapidly from 1% at 5 keV to unity at 8 keV; at 10 keV the *ACIS-S3* background is about 20 times higher than the source. *MOS* and *pn* ratios rise above 1% around 7 keV and remain below 30% and 10% respectively at all energies.

The outline of the paper is as follows: in Sect. 2 we provide details on our data preparation; in Sect. 3 we describe results from the spectra analysis; in Sect. 4 we compare results from the analysis of *EPIC* data with those from *Chandra*; in Sect. 5 we discuss our results and in Sect. 6 we summarize them. We assume $H_0 = 70$ km s^{-1} Mpc^{-1} so that 1 arcsec = 0.35 kpc at the redshift of NGC1275 (0.0176, Huchra et al. 1999); all errors are 1σ unless otherwise stated.

2. Data preparation

Perseus was observed by *XMM-Newton* during revolution 1125 with the *EPIC MOS* (*pn*) detectors in Full Frame Mode
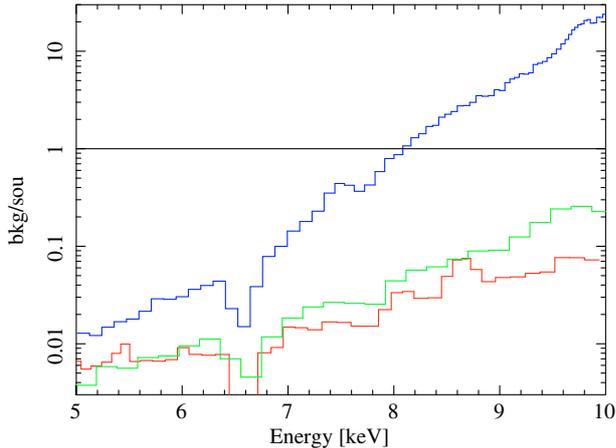
Fig. 1. Ratio of background to source spectra for the *ACIS-S3* (blue), *MOS2* (green) and *pn* (red) instruments from the 1′–2′ ring. The *ACIS-S3* ratio rises rapidly from 1% at 5 keV to unity at 8 keV; at 10 keV the *ACIS-S3* background is about 20 times higher than the source. *MOS* and *pn* ratios rise above 1% around 7 keV and remain below 30% and 10% respectively at all energies.

(Extended Full Frame) with medium filter on all *EPIC* cameras. We have obtained calibrated event files for the *MOS1*, *MOS2* and *pn* cameras using SAS version 7.1 "Emchain", "Epchain" tasks and calibration files (CCFs) available at the end of August 2007. A soft proton cleaning procedure was performed by extracting a light curve in 100 s bins in the 10–12 keV energy band in a peripheral region of the *MOS* and *pn* cameras and applying a threshold of 0.20 cts s^{-1} for *MOS* and 0.6 cts s^{-1} for *pn*, to generate a filtered event list. The total live time after screening is 1.12×10^5 s for *MOS1* and *MOS2* and 6.6×10^4 for *pn*. Finally, we filtered event files according to FLAG (FLAG==0) and PATTERN (PATTERN≤4 for *pn* and PATTERN==0 for *MOS*). The filtered event files, which were subsequently used for data analysis, contained a total of about 16×10^6, 19×10^6 and 35×10^6 events for *MOS1*, *MOS2* and *pn* respectively.

2.1. Spectra preparation

We have accumulated spectra from annuli with bounding radii 0.5′–1′, 1′–2′ and 2′–3′, and from sectors 45 degrees wide from the same annuli.

As already pointed out in Sect. 2, for the *MOS* detectors only PATTERN==0 events were selected, this was done to avoid pile up which, albeit small (few %), can have non-negligible consequences within ~2′ from the cluster core (i.e. be sufficiently strong to distort the spectral shape, particularly at high energies, Molendi & Sembay 2003). We generate flux weighted effective areas using the arfgen task with exposure corrected images of the source and the parameter extended source switched to true. We also correct *pn* spectra for out of time events following the prescriptions of Grupe (2001). Redistribution matrices were generated with the rmfgen task, one matrix was generated for *MOS1* and *MOS2* respectively, a set of 10 matrices were generated for *pn* to account for the dependence of the *pn* spectral resolution upon the distance to the camex.

Although Perseus is the brightest cluster in the X-ray sky and *EPIC* offers the largest effective area of any X-ray experiment flown thus far, a reliable characterization of the background is one of the fundamental requirements to carry out a search for non-thermal emission. Our background subtraction

procedure makes use of a sum of blank fields selected by our own group (Leccardi & Molendi 2008). Spectra have been accumulated from the same sky regions as the source spectra, after re-projection onto the sky attitude of the source. To allow for differences in the intensity of the background components between source and background observations we re-normalize the background spectra. The re-normalization constant is determined by comparing the intensity of the total emission in source and background observations from a peripheral region and in a hard (10–12 keV for *MOS1* and *MOS2*, 12–14 keV for *pn*) energy band where source emission is expected to be small. The re-normalization constants, R_k, are found to be 1.64, 1.57 and 1.52 for *MOS1*, *MOS2* and *pn* respectively. To verify the correctness of our procedure we performed a spectral fit to the data in the outer ring used to determine the re-normalization constants, the fit was performed in a hard, albeit source dominated band (4–7 keV). The best fitting model was then extrapolated to a background dominated band (8–14 for *pn* and 8–12 for *MOS*) where it was found to reproduce adequately the source spectrum. Variations of the re-normalization constant described above of only a few percent result in a best-fitting model extrapolation significantly under or over-shooting the source spectrum, indicating that our determination of the re-normalization constants is good to a few percent. To account for possible variations in the background intensity over the detectors and the issuing re-normalization errors on the background subtraction we have assumed a 5% systematic uncertainty on the re-normalization constants we apply on all our source spectra. In practice this is achieved by performing 3 different fits for each spectrum one with the background with the standard re-normalization constant, R_k, the other two with a higher $R_k + 0.05 \times R_k$, and lower, $R_k - 0.05 \times R_k$, re-normalization constants respectively.

As a further check of the quality of our background subtraction technique we have also pursued a different venue, i.e. background modeling, following the lines described in a recent paper (Leccardi & Molendi 2008). A comparison of results obtained with the two methods shows that within some 4 arcmin of the cluster core they provide virtually indistinguishable results. Given that the background modeling alternative is more cumbersome from the point of view of the spectral analysis and that it has only been developed for the *MOS* detectors (Leccardi & Molendi 2008) in the following we report results obtained with the background subtraction method.

One of the hallmarks of the Perseus observations is its high statical quality, typical spectra contain in the order of hundred of thousands to millions of source counts. Under these extreme conditions statistical errors can be minuscule, especially around 1 keV where effective areas peak: here systematic errors become an important if not dominant component of the error budget. This can be readily verified by inspecting spectral fits, typically residuals appear at the position of edges where rapid variations in the effective areas occur. Conversely far less statistics is available in the 5–10 keV band where some astrophysical features, such as the thermal exponential cutoff, Fe and Ni emission lines are located. The question is then how to prevent the χ^2 fitting procedure from giving more importance to statistically significant spurious features located around 1 keV than to astrophysical signatures at higher energies. We adopt two independent methods: the first is to identify the cause of systematic errors and evaluate their impact on parameter estimates; the second is to associate a systematic error to spectra. While the former strategy may be considered as part of the modeling process of Perseus spectra, and as such will be described in detail in the following section, the latter is accomplished by associating a

systematic error to all spectral bins. We choose a somewhat moderate and energy independent value of 2% for the systematic error for three reasons: firstly it is consistent with a conservative estimate for the relative calibration of the *EPIC* instruments (Kirsch & EPIC-Consortium 2007); secondly it has the effect of increasing errors in the low energy part of the spectrum to the point that they become comparable to errors at higher energies; thirdly a detailed energy dependent characterization of systematic errors is in part achieved through the modeling processes described in the following section and in part by associating the same relative systematic error to spectral regions characterized by very different statistical errors as already clarified in the previous point. Inclusion of the systematic error is technically achieved by modifying the SYS_ERR keyword in the source spectra header. The XSPEC package associates to each spectral bin an error which is the sum in quadrature of the statistical and systematic error.

3. Spectral analysis

Due to its higher effective area we have considered the *pn* camera as lead instrument in our analysis. Results from the analysis of *MOS* data is also reported (see Sect. 3.1.2). We have made use of two kind of baseline models: a two temperature plus power-law model, in XSPEC jargon phabs*(2vmekal+pegpwrlw), which we shall refer to as 2TP, and a multi temperature plus power-law model, phabs*(5vmekal+pegpwrlw), hereafter MTP. For the former model the free parameters are the $N_{\rm H}$, the temperatures, the normalizations of the thermal and pow-law components, the redshift, the O, Mg, Si, S, Ar, Ca, Fe and Ni abundances. Ne, Na and Al abundances are tied to O; metal abundances for a given species of one component are tied to those of the other; the photon index of the power-law is fixed to 1.8, one of the values adopted in Sanders et al. (2005) and Sanders & Fabian (2007). For the latter model the free parameters are the $N_{\rm H}$, the normalizations of the thermal and power-law components, the redshift, the O, Mg, Si, S, Ar, Ca, Fe and Ni abundances. Ne, Na and Al abundances are tied to O; metal abundances for a given species of one component are tied to those of the others. The five temperatures, which are fixed, are $kT_1 = 0.5$ keV, $kT_2 = 1.0$ keV, $kT_3 = 2.0$ keV, $kT_4 = 4.0$ keV and $kT_5 = 8.0$ keV, the power-law index, as for the 2TP model, is fixed to 1.8. Throughout our analysis we adopt solar units according to Anders & Grevesse (1989).

Spectral fits are conducted in the 0.5–11 keV band for both *MOS* and *pn*. The low energy cutoff is enforced to avoid residual calibration (Kirsch & EPIC-Consortium 2007) and cross-calibration (Stuhlinger et al. 2008) problems, moreover the relatively high column density towards the Perseus cluster reduces significantly the value of data accumulated at the softest energies.

3.1. Analysis in rings

We investigate a region within 3′ from the emission peak, where evidence of non-thermal emission has been found with *Chandra* (Sanders & Fabian 2007, and references therein). We consider spectra in 3 annuli with bounding radii: 0.5′–1.0′, 1.0′–2.0′ and 2.0′–3.0′. We exclude the region within 0.5′ from the emission peak to avoid contamination from the AGN.

From the analysis of the *Chandra* data (Sanders & Fabian 2007, and references therein) we expect the putative non-thermal component to make up no more than 10–20% of the total emission, even at high energies where its relative contribution is

Table 1. Parameters from the *pn* 1′–2′ spectrum fits.

Model	$Z_{\rm Fe}^a$	$Z_{\rm Fe}^a$	$S_{\rm NT}^b$	χ^2	d.o.f.
2TP-nosys	0.53 ± 0.01	—	4.3 ± 0.3	1540	509
MTP-nosys	0.53 ± 0.01	—	3.7 ± 0.5	1489	508
2TP	0.48 ± 0.01	—	1.6 ± 0.3	636	509
MTP	0.50 ± 0.01	—	1.9 ± 0.3	631	508
2TP-gs	0.50 ± 0.01	—	1.5 ± 0.8	453	509
MTP-gs	0.52 ± 0.01	—	1.7 ± 0.7	449	508
2TP-gs-2Fe	0.63 ± 0.06	0.47 ± 0.02	1.1 ± 0.8	447	508
MTP-gs-2Fe	0.79 ± 0.10	0.49 ± 0.01	1.3 ± 0.7	437	507

Notes: ^{a} Fe abundance in solar units according to Anders & Grevesse (1989). ^{b} Surface brightness in units of 10^{-16} erg cm^{-2} s^{-1} arcsec^{-2} in the 2–10 keV band.
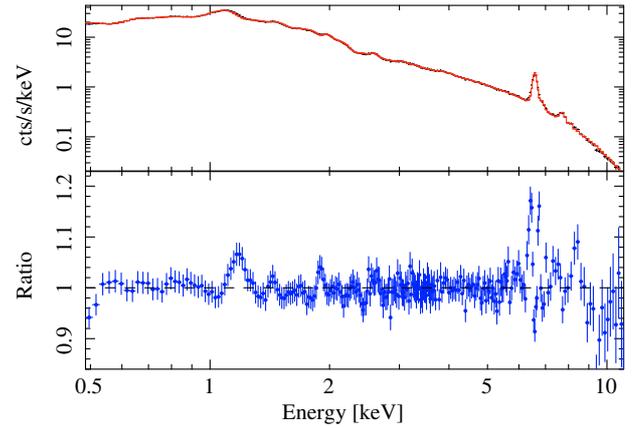
Fig. 2. Best fit with the 2TP model to the *pn* spectrum in the 1′–2′ ring. *In the top panel* we show the spectrum, in black, and the best fitting model in red. *In the bottom panel* we show residuals in the form of a ratio of the data over the model.

largest. Under such conditions a meticulous analysis of the data is mandatory. We begin by considering the annulus with bounding radii 1′–2′.

3.1.1. The 1′–2′ ring

A fit to the *pn* data with the MTP model returns values of the surface brightness of the non-thermal component, $S_{\rm NT}$, of $(1.9 \pm 0.3) \times 10^{-16}$ erg cm^{-2} s^{-1} arcsec^{-2}, the 2TP model returns a similar value of $(1.6 \pm 0.3) \times 10^{-16}$ erg cm^{-2} s^{-1} arcsec^{-2} (see also Table 1). Interestingly a fit of the MTP and 2TP models on the *pn* spectrum with no systematic errors applied, hereafter MTP-nosys and 2TP-nosys, returns higher values for the non-thermal component surface brightness (see Table 1).

Inspections of the best-fit residuals reveals three major features, namely: an excess around 1.2 keV; a substantial structure around the Fe Kα line and an excess around 8.3 keV (see Fig. 2). The 1.2 keV excess is located in the blue wing of the Fe L-shell blend and is most likely due to an inaccurate modeling of the L-shell transitions within the mekal code. Indeed fitting with the apec rather than the mekal code results in a substantial reduction of the residuals, with no significant modification of the best fit parameters. The excess around 8.3 keV is due to background subtraction inaccuracies. We remind our readers that in the *pn* camera the region around 8 keV is populated by fluorescence lines of instrumental origin which are not easily subtracted. Fortunately the contamination in the 1′–2′ region is only mild (Ehle et al. 2007) and the ensuing

systematics are relatively modest. A further mitigating factor is the relatively large statistical error associated to the source spectrum above ~7 keV. The structure around the Fe Kα line is due to an incorrect modeling of the *pn* spectral resolution within the redistribution matrix. From the analysis of *pn* spectra from a sample of clusters (De Grandi & Molendi 2008, in preparation) we have found that the above resolution miss-calibration can be compensated for by including a multiplicative component that performs a Gaussian smoothing of the spectral model (gsmooth in XSPEC). We set the width of the gaussian kernel to be 4 eV (*FWHM*) at 6 keV and assume a power-law dependency of the width on the energy with an index of −1. Both the MTP and 2TP models modified with the gsmooth component, hereafter MTP-gs and 2TP-gs respectively, provide a substantially better fit than their non-modified counterparts ($\Delta\chi^2 \sim 200$). The surface brightness of the non-thermal component is essentially unchanged with respect to the previous fits both for the MTP-gs, $S_{\mathrm{NT}} = (1.7 \pm 0.7) \times 10^{-16}$ erg cm^{-2} s^{-1} arcsec^{-2} and 2TP-gs model $S_{\mathrm{NT}} = (1.5 \pm 0.8) \times 10^{-16}$ erg cm^{-2} s^{-1} arcsec^{-2}.

A further modification concerns the treatment of the Fe abundance. When fitting multi-phase models it is customary to tie the abundances of the different phases; this solution is adopted because in most cases it is impossible to derive independent metal abundance measures. In the case at hand it is possible to have two largely independent measurements of the Fe abundance, one for the hot phase, contributing mainly to the K-shell line emission, and the other for the cool phase dominating the L-shell blend emission. We recall that, for most cool core clusters, spatially resolved analysis shows that the Fe abundance anti-correlates with temperature (i.e. Fig. 11 of Sanders et al. 2004, for the Perseus cluster). We have modified our two test models to allow for different Fe abundances in the cool and the hot phase. For the 2TP-gs model we simply decouple the Fe abundance of the two components while for the MTP-gs model we define two Fe abundances: one for the cool i.e. 0.5, 1.0 and 2.0 keV components and the other for the hot, i.e. 4.0 and 8.0 keV components. As expected for both models, hereafter 2TP-gs-2Fe and MTP-gs-2Fe, the Fe abundance for the cool phase or phases is higher ($Z_{\mathrm{Fe}} = 0.63 \pm 0.06$ and $Z_{\mathrm{Fe}} = 0.79 \pm 0.10$ respectively) than for the hot phase ($Z_{\mathrm{Fe}} = 0.47 \pm 0.02$ and $Z_{\mathrm{Fe}} = 0.49 \pm 0.01$ respectively). Both the MTP-gs-2Fe and 2TP-gs-2Fe models provide a better fit than their single Fe abundance counterparts although the improvement is not a dramatic one ($\Delta\chi^2 \sim 10$). The surface brightness of the power-law component is found to be $S_{\mathrm{NT}} = (1.1 \pm 0.8) \times 10^{-16}$ erg cm^{-2} s^{-1} arcsec^{-2} for the 2TP-gs-2Fe model and $S_{\mathrm{NT}} = (1.3 \pm 0.7) \times 10^{-16}$ erg cm^{-2} s^{-1} arcsec^{-2} for the MTP-gs-2Fe model. In retrospect it is fairly easy to understand why the decoupling of hot and warm phase Fe abundances entails somewhat lower intensities for the non-thermal component. A high temperature component ($kT \sim 8$ keV) over a small energy range is rather similar to a power-law component, the major discriminant being of-course the line emission. If the high temperature component is forced to have a metal abundance that is higher than the true one it will not be able to reproduce the continuum correctly, such an excess continuum will be well modeled by a power-law component.

We may summarize our results by stating that while the addition of systematic errors to the spectrum results in a reduction of the intensity of the power-law component of a factor of 2, the introduction of some modifications to our base-line models 2TP and MTP, either to improve the description of the astrophysical scenario or to account for residual calibration problems, does not result in substantial modifications of the intensity of the non-thermal component.

Table 2. Parameters from the *MOS1* 1′–2′ spectrum fits.

Model	Z_{Fe}^a	Z_{Fe}^a	S_{NT}^b	χ^2	d.o.f.
2TP-nosys	0.66 ± 0.02	—	5.4 ± 1.0	951	553
MTP-nosys	0.63 ± 0.01	—	4.2 ± 0.5	1009	552
2TP	0.62 ± 0.02	—	3.8 ± 1.1	593	553
MTP	0.59 ± 0.01	—	3.0 ± 0.9	599	552
2TP-2Fe	0.67 ± 0.04	0.53 ± 0.05	2.7 ± 1.4	591	552
MTP-2Fe	0.66 ± 0.08	0.58 ± 0.02	3.0 ± 0.9	598	551
2TP-2Fe-gf	0.67 ± 0.05	0.54 ± 0.05	2.7 ± 1.5	611	551
MTP-2Fe-gf	0.71 ± 0.12	0.58 ± 0.02	2.4 ± 1.3	592	550

Notes: [a] Fe abundance in solar units according to Anders & Grevesse (1989). [b] Surface brightness in units of 10^{-16} erg cm^{-2} s^{-1} arcsec^{-2} in the 2–10 keV band.

Table 3. Parameters from the *MOS2* 1′–2′ spectrum fits.

Model	Z_{Fe}^a	Z_{Fe}^a	S_{NT}^b	χ^2	d.o.f.
2TP-nosys	0.63 ± 0.01	—	7.4 ± 0.4	1066	555
MTP-nosys	0.56 ± 0.01	—	2.6 ± 0.5	1228	554
2TP	0.61 ± 0.02	—	4.2 ± 1.5	635	555
MTP	0.55 ± 0.01	—	3.4 ± 0.7	657	554
2TP-2Fe	0.65 ± 0.04	0.37 ± 0.10	2.8 ± 1.5	632	554
MTP-2Fe	0.71 ± 0.07	0.52 ± 0.03	2.9 ± 0.8	655	553
2TP-2Fe-gf	0.74 ± 0.13	0.49 ± 0.07	3.6 ± 1.7	611	553
MTP-2Fe-gf	0.80 ± 0.15	0.52 ± 0.02	2.9 ± 1.5	615	552

Notes: [a] Fe abundance in solar units according to Anders & Grevesse (1989). [b] Surface brightness in units of 10^{-16} erg cm^{-2} s^{-1} arcsec^{-2} in the 2–10 keV band.

To assess how different choices for the power-law slope impact on the estimate of the surface brightness of the non-thermal component we have rerun fits with slopes of $\Gamma = 1.5$ and $\Gamma = 2.0$. We find that surface brightnesses are somewhat lower (higher) for $\Gamma = 1.5$ ($\Gamma = 2.0$). For instance, in the case of the MTP-gs-2Fe model, the surface brightness is $S_{\mathrm{NT}} = (1.2 \pm 0.8) \times 10^{-16}$ erg cm^{-2} s^{-1} arcsec^{-2} and $S_{\mathrm{NT}} = (2.0 \pm 0.8) \times 10^{-16}$ erg cm^{-2} s^{-1} arcsec^{-2} respectively for the $\Gamma = 1.5$ and $\Gamma = 2.0$ choices. To gauge the effect of systematic errors on our fitting procedure we have experimented with values ranging from 0% to 4%. For the MTP model we find that the surface brightness of the non-thermal component steadily decreases from $(3.7 \pm 0.5) \times 10^{-16}$ erg cm^{-2} s^{-1} arcsec^{-2} for no systematic error to $(1.2 \pm 0.3) \times 10^{-16}$ erg cm^{-2} s^{-1} arcsec^{-2} for a 4% systematic error. To verify whether spatial resolution plays a role in the determination of the power-law surface brightness we have analyzed spectra from circular sectors. For the 1–2 arcmin annulus we consider 8 equally spaced sectors each 45 degrees wide. Analysis of the sectors provides results similar to those found in rings albeit with a somewhat reduced statistics.

3.1.2. The *MOS* spectra for the 1′–2′ ring

As anticipated we have used *MOS1* and *MOS2* spectra to verify *pn* results. A fit with the simple MTP and 2TP models returns values of the surface brightness of the non-thermal component between 3 and 4 × 10^{-16} erg cm^{-2} s^{-1} arcsec^{-2}, (see Tables 2 and 3 for details). These values are in agreement with each other and somewhat in excess of those obtained with the *pn*. Fits on the *MOS1* and *MOS2* spectra with no systematic errors applied, dubbed 2TP-nosys and MTP-nosys, resulted in a higher value of the χ^2; the surface brightness of the non-thermal component is also generally higher, however this not always the case

(see Tables 2 and 3 for details). Decoupling of the hot and cool phase Fe abundances results in changes similar to those observed for the *pn*: the χ^2 suffers a modest decrease; the hot phase Fe abundance is found to be lower than the cool phase Fe abundance and the surface brightness of the non-thermal component does not vary substantially. Inspection of the residuals shows that the *MOS1* and *MOS2* Fe Kα lines are not broader than the one included in the best fitting model, consequently we refrain from applying a smoothing component to the spectral model. Conversely we find evidence of some residual non-linearity in the energy scale calibration, particularly in the *MOS2* spectrum. We have compensated for this effect by allowing for a constant shift in the energy scale, this is achieved within XSPEC by performing a `gain fit` on the best fit model, fixing the linear parameter to 1 and leaving the offset parameter free. From the resulting best fits, which we refer to as 2TP-2Fe-gf and MTP-2Fe-gf, we detect a shift of about 2 eV for *MOS1* and 6 eV for *MOS2*, other best fit parameters are not substantially different from those measured from the previous set of fits (see Tables 2 and 3 for details).

As for *pn* spectra we have experimented with different values for the power-law slopes, the systematic error and performed analysis of spectra in sectors. Our findings are similar to those reported for the *pn* spectra in as far as the power-law slope and analysis in sectors is concerned. There are some differences regarding systematic errors. For the *MOS2* detector, unlike for the *MOS1* and *pn* detectors, inclusion of a systematic error results in a reduction of the non-thermal component surface brightness only for values of the error higher than 3%.

3.1.3. Comparison between *pn* and *MOS* estimates

Comparing results for *MOS1* and *MOS2* with those from *pn* we find that the surface brightness of the non-thermal component gauged with the former experiments is somewhat higher than that measured with the latter, however, for most measures, the differences are comparable to the errors associated to individual measurements. More specifically, if we exclude measurements without correction for systematic errors we find that *pn* measures are roughly contained between 1×10^{-16} erg cm^{-2} s^{-1} arcsec^{-2} and 2×10^{-16} erg cm^{-2} s^{-1} arcsec^{-2} and *MOS* measures between 2×10^{-16} erg cm^{-2} s^{-1} arcsec^{-2} and 4×10^{-16} erg cm^{-2} s^{-1} arcsec^{-2}.

If we consider measurements with no correction for systematics (i.e. MTP-nosys bst fits) we find that typical errors, 0.5×10^{-16} erg cm^{-2} s^{-1} arcsec^{-2}, are substantially smaller than the spread of values described above, indicating that systematic uncertainties afford the dominant contribution to the error budget. Under these circumstances providing a statistically meaningful confidence range for our measurement of the surface brightness of the non-thermal component is rather difficult, particularly since the approach we have adopted to incorporate systematic errors is of a heuristic nature. We therefore resort to an alternative and less ambitious approach: we make use of the spread of values measured for the different models and different experiments to provide a loose range for the surface brightness of the non-thermal component, namely $0-5 \times 10^{-16}$ erg cm^{-2} s^{-1} arcsec^{-2}. It is perhaps ironic that a meticulous analysis of the data, such as the one reported here, has lead to an uncommonly loose estimate of the non-thermal component, however, as long as we do not dispose of statistical tools allowing us to incorporate systematic uncertainties in analysis such as these, our options are rather limited.
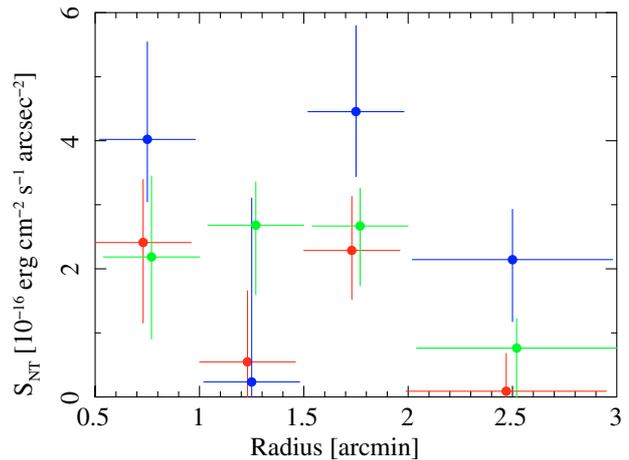
Fig. 3. Radial profile for the surface brightness of the non-thermal component for the three *EPIC* cameras: *pn* is red, *MOS1* is blue and *MOS2* is green. Radii have been slightly offset to improve readability.

The results we report here are at variance with those that we presented at a conference in Garching in August 2006, essentially 4 factors have lead to these differences. The factors are: a new release of the *MOS* quantum efficiency curves in August 2007 leading to a substantial improvement of the *MOS* vs. *pn* cross-calibration and to a revision of *MOS* spectral analysis results; use of `PATTERN==0` events only for *MOS* spectra; a more accurate treatment of the background following some recent work within our group (Leccardi & Molendi 2007, 2008); a novel treatment for systematic effects.

3.2. Radial profile

In Fig. 3 we show the radial profile for the surface brightness of the non-thermal component. The profile is based on the analysis of spectra accumulated in annuli with bounding radii: 0.5′–1.0′, 1.0′–1.5′, 1.5′–2.0′ and 2.0′–3.0′, note that the 1.0′–2.0′ annulus has been split in two to improve the resolution of the profile. The reported surface brightnesses have been estimated using the MTP-gs-2Fe model for *pn* and MTP-2Fe-gf model for *MOS1* and *MOS2*.

All measurements lie between 0 and 5×10^{-16} erg cm^{-2} s^{-1} arcsec^{-2}. For the innermost ring the *EPIC* mean value for the surface brightness of the non-thermal component is $(2.4 \pm 1.0) \times 10^{-16}$ erg cm^{-2} s^{-1} arcsec^{-2}, while for the 1.5′–2.0′ annulus we find $S_{\mathrm{NT}} = (2.3 \pm 0.9) \times 10^{-16}$ erg cm^{-2} s^{-1} arcsec^{-2}.

We have verified that similar measurements are obtained when fitting spectra with slightly different spectral models, i.e. all *pn* measurements obtained with the MTP-gs model are within 1σ of those reported in Fig. 3, similarly all *MOS1* and *MOS2* measures obtained with the MTP-2Fe model are within 1σ of those reported in Fig. 3.

Assuming a rather conservative approach, we might say that the surface brightness of the non-thermal component is somewhere between 0 and 5×10^{-16} erg cm^{-2} s^{-1} arcsec^{-2}. This is in agreement with what we found from the analysis of the 1.0′–2.0′ annulus (see Sect. 3.1.3) and may therefore be considered as a general result of our analysis.

**Table 4.** Parameters from the *Chandra ACIS-S3* 1′–2′ spectrum fits.

Model	Z_{Fe}^a	Z_{Fe}^a	S_{NT}^b	χ^2	d.o.f.
2TP-nosys	0.81 ± 0.01	—	$10.3^{+0.4}_{-0.3}$	2358	522
MTP-nosys	0.79 ± 0.01	—	$8.8^{+0.3}_{-0.2}$	2360	521
2TP	$0.73^{+0.03}_{-0.02}$	—	$8.4^{+0.8}_{-0.6}$	589	522
MTP	$0.74^{+0.03}_{-0.02}$	—	$8.6^{+0.5}_{-1.0}$	584	521
2TP-2Fe	$0.95^{+0.10}_{-0.08}$	0.68 ± 0.03	$7.8^{+1.3}_{-0.7}$	582	521
MTP-2Fe	$1.20^{+0.65}_{-0.13}$	$0.67^{+0.03}_{-0.02}$	$7.1^{+1.3}_{-0.7}$	578	520

Notes: ^{a} Fe abundance in solar units according to Anders & Grevesse (1989). ^{b} Surface brightness in units of 10^{-16} erg cm^{-2} s^{-1} arcsec^{-2} in the 2–10 keV band.

4. Comparison with *Chandra*

In an attempt to understand the origin of the difference between our measurements and those based on *Chandra* data, we have reduced and analyzed the longest *ACIS-S* observation (see Fabian et al. 2006, Table 1). The data were reduced with the X-ray analysis packages *CIAO* 3.4 and *Heasoft* 6.4 in conjunction with the *Chandra* calibration database (*Caldb*) version 3.4.2 (using gainfile acisD2000-01-29gain_ctiN0006.fits). To ensure the most up-to-date calibration, all data were reprocessed from the "level 1" events files, following the standard *Chandra* data-reduction threads[1]. We applied the standard corrections to account for a time-dependent drift in the detector gain and charge transfer inefficiency, as implemented in the *CIAO* tools. From low surface brightness regions of the active chips we extracted a light-curve (5.0–10.0 keV) to identify and excise periods of enhanced background. The spectra were re-binned to ensure a S/N of at least 3 and a minimum 20 counts per spectral bin. Spectral fits, using both 2TP and MTP models provide values consistent with those derived by Sanders & Fabian (2007) (see their Fig. 20) and well in excess of those measured with *EPIC* (see Table 4). We have included a 2% systematic error to the *Chandra* spectrum, as done for the *EPIC* spectra, without noticeable effects on the non-thermal component, or any other spectral parameter. The background file represents well the background in the actual observation, as gauged by the 9–13 keV band count-rate and even if we experiment changing the normalization by ±5% the flux in the power-law component is comparable with the one measured with the background at the nominal value (7.6 ± 0.7 and $8.9^{+0.5}_{-0.8}$, in the units of Table 4 and using the MTP model, in the two cases). We investigated possible variations in the set of Perseus observations reducing other long observations, namely OBS-ID 4948 and OBS-ID 4289, in particular the latter provides an important double check because it was performed at an earlier epoch and with a different level of low-energy degradation. We did not find any difference within the errors for the value of the spectral parameters and in particular of the non-thermal component between the different observations.

In an attempt to understand the difference between *Chandra* and *XMM-Newton* measurements, we have compared the *EPIC-pn* spectrum accumulated in the 1′–2′ annulus with the *Chandra* spectrum extracted from the same region. Technically this has been done by plotting the *pn* and the *ACIS-S3* residuals with respect to the *pn* MTP-gs-2Fe best-fit model in the form of a ratio of the data over the model. A 5% re-normalization has been applied to the *Chandra* spectrum to facilitate the comparison with the *pn* spectrum. Interestingly the *ACIS-S3* spectrum is significantly harder than the *EPIC-pn* spectrum. As shown in Fig. 4,

[1] http://cxc.harvard.edu/ciao/threads/index.html
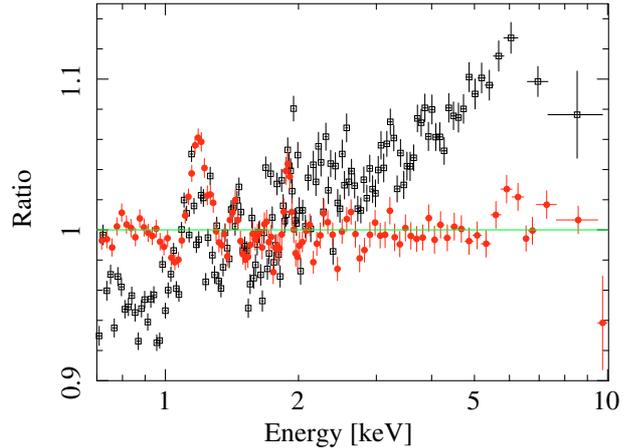
Fig. 4. Ratio of the *ACIS-S3* (black) and *pn* (red) spectra accumulated in the 1′–2′ annulus over the best fitting MTP-gs-2Fe *pn* model. A re-normalization constant of 4.8% has been applied to the *ACIS-S3* spectrum.

while at 2 keV the two spectra have by construction the same intensity, at 5 keV the *Chandra* spectrum is in excess of the *EPIC-pn* spectrum by about 10%. The discrepancy is rather significant, considering that the non-thermal component intensity is of the same order. A comparison of the *pn* spectrum with the *MOS1* and *MOS2* spectra similar to the one reported in Fig. 4 shows that in the 1–7 keV range both *MOS1* and *MOS2* spectra are within a few % of the *pn* spectrum. We refrain from plotting the *MOS* spectra in Fig. 4 simply to avoid overcrowding.

Since the background of the *ACIS-S3* and *EPIC* cameras at energies below 5 keV is extremely small (see Fig. 1), the most likely origin for the difference is a cross-calibration issue on the effective areas in the 1–5 keV range. Interestingly cross-calibration activities conducted by a number of workers (see David et al. 2007), mostly on cluster spectra, also point to a discrepancy between *Chandra* and *XMM-Newton* measurements. For hot clusters, ($kT \gtrsim 5$ keV) *Chandra* spectra typically return higher temperatures than *EPIC* spectra (see David et al. 2007, figure on page 2). Further investigations have revealed that the discrepancy likely results from problems in the calibration of the *Chandra* high energy effective areas. David et al. (2007) show that measuring the temperature of A2029 from the ratio of the He-like over H-like Kα lines and comparing the resulting continuum model with the observed spectrum, the latter is flatter than the former. More specifically, if the model is normalized to the observed spectrum at energies higher than 5 keV, the latter is found to be about 8% below the model at 2 keV. This discrepancy is remarkably similar to the one we find when comparing the *pn* and *ACIS-S3* spectrum of Perseus (see Fig. 4).

5. Discussion

From a general perspective our analysis may be viewed as an attempt to characterize the spectrum of an X-ray source beyond a simple one/two component model. Given the modest intensity of the component we are specifically interested in and the lack of spectral signatures, such as lines or edges, the task is by no means a trivial one. Clearly it can only be attempted on sources where adequate statistics is available. It is often the case that, when the statistics is abundant, systematics become the dominant source of error. At the present time X-ray astronomers do not have a standard method of analyzing data under these

predicaments and mostly resort, has we have done, to a trial and error approach. The development of a standard strategy, possibly descending from first principles, is highly desirable particularly if we consider that in the not too distant future X-ray missions such as *XEUS* or *Con-X* will have, as one of their primary goals, the detailed characterization of relatively bright X-ray spectra. In some instances the advent of high resolution spectrometry will provide a valid solution. In others, where features that need to be characterized are broad, either because they are of non-thermal nature, such as the putative hard tails in clusters, or because they are smeared by other processes (i.e. the broad iron line observed in nearby AGN), solutions will have to be found elsewhere. Recent work by Drake et al. (2007) provides an interesting starting point.

5.1. EPIC *estimate*

In this paper we have characterized the surface brightness of the non-thermal component in Perseus by resorting to a heuristic approach which can be divided in 2 steps: 1) inclusion of 2% systematic errors on spectra; 2) modification of spectral models. As far as the first step is concerned, we find a significant reduction of the surface brightness measured from the *pn* spectra when the 2% systematic error is included, no significant changes are found for the *MOS* measurements (note however that a reduction is observed starting from a 3% systematic error, see Sect. 3.1.2). As far as the second step is concerned, the stability of our results with respect to the inclusion of corrections for some imperfections in redistribution matrix, effective area, energy scale and choice of astrophysical model indicate that our measures are relatively robust with respect to the residual systematic effects we have been able to identify. Comparison of *MOS* with *pn* results shows that the former favour a somewhat higher value for the surface brightness of the non-thermal component than the latter, roughly speaking 2 against 1. The difference between the two measures is most likely caused by minor cross-calibration issues, possibly in the high energy response of either *MOS* or *pn*. Since we do not have firm evidence as to which of the two experiments is better calibrated, rather than privileging measures from one over the other, we take the common envelope of *MOS* and *pn* measurements (i.e. $0-5 \times 10^{-16}$ erg cm^{-2} s^{-1} arcsec^{-2}) as our best estimate for the interval constraining the surface brightness of the non-thermal component. Some of our readers might find this range rather broad, particularly in light of the high statistical quality of our data, we reiterate that the major source of indetermination here as elsewhere are systematic and not statistical errors.

5.2. EPIC *vs.* ACIS

Results from the analysis of *EPIC* spectra, either *pn* or *MOS*, cannot be reconciled with those obtained with *ACIS-S3*. As discussed in Sect. 4 the difference is to be ascribed to a cross-calibration issue between *EPIC* and *ACIS*. Similar problems have been identified by a group of calibrators who have compared *Chandra* and *XMM-Newton* observations of hot clusters (David et al. 2007). Recent efforts by *Chandra* calibrators (David et al. 2007; Jerius et al. 2008) have shown that the above difference follows from problems in the calibration of the *Chandra* high energy effective areas.

5.3. Magnetic field estimates

Under the assumption that the non-thermal emission originates from inverse Compton (IC) scattering of seed microwave and infrared photons by relativistic electrons, responsible of the synchrotron emission in the mini radio-halo, the Perseus core magnetic field can be estimated from the energy density of the seed photon field, $U_{\rm rad}$, the synchrotron and inverse-Compton luminosities, L_R and L_X, i.e. $U_B = U_{\rm rad} \cdot L_R/L_X$, where U_B is the energy density of the magnetic field. Sanders et al. (2005), from their measures of the non-thermal component, find magnetic field intensities ranging from several μG at the very center, to ~1.0 μG at 8 kpc (0.4′) and ~0.1 μG at 40 kpc (2′) (see Fig. 9 of Sanders et al. 2005). Our measurements can be used to provide a revised estimate of the B field. As discussed above we estimate the surface brightness of the non-thermal component to be somewhere between 0 and 5×10^{-16} erg cm^{-2} s^{-1} arcsec^{-2}. We therefore start by assuming an upper limit of 5×10^{-16} erg cm^{-2} s^{-1} arcsec^{-2}, from this we subtract a value of 2.4×10^{-16} erg cm^{-2} s^{-1} arcsec^{-2}, as in Sanders et al. (2005), to account for projection effects. The resulting surface brightness is used to derive lower limits for the magnetic field using essentially the same method and radio measures described in Sanders et al. (2005). In the 0.5′–1′ and 1′–2′ annuli our X-ray estimate convert into lower limits of roughly 0.4 μG and 0.3 μG respectively. We note that these numbers have been derived through a series of rather drastic approximations, (i.e. we have a rather poor determination of the X-ray upper limit, the radio emission is measured at a frequency which is substantially higher than that at which non-thermal electrons responsible for the inverse Compton emission emit via synchrotron, the B field is assumed to be constant, etc.) what really matter is that they are lower limits and not detections.

Faraday rotation measures (RM) in cool cores on scales of tens of kpc are in the order of several hundreds to thousands (Taylor et al. 2002). Estimates of magnetic fields from rotation measures have undergone some revision in the last few years with more recent estimates typically in the order of a few μG (Clarke 2004; Enßlin & Vogt 2006). In the case of the Perseus mini radio-halo Faraday rotation measures are available only on very small scales (Taylor et al. 2006), i.e. few tens of pc. RM estimates are in the order of ~7000 rad m^{-2} leading to B field values of ~25 μG under the assumption the screen is localized in the ICM. This, however, appears to be unlikely as variations of 10% in the RM are observed on scales of ~1 pc (Taylor et al. 2006), while ICM magnetic fields are expected to be ordered on significantly larger scales (few kpc: Taylor et al. 2002; Vogt & Enßlin 2005; Enßlin & Vogt 2006). Application of the classical minimum-energy argument to the Perseus mini radio-halo data, leads to estimates for the central (i.e. $r = 0$) magnetic field strength of ~7 μG (Pfrommer & Enßlin 2004).

IC estimates of the magnetic field based on *Chandra* measurements (Sanders et al. 2005) are about an order of magnitude below the RM and minimum-energy estimates detailed above. A similar discrepancy has been found when comparing magnetic field estimates on cluster wide scales. There IC measures are in the 0.2–1 μG range (Rephaeli et al. 2008, and references therein), while RM estimates are about an order of magnitude larger (e.g. Carilli & Taylor 2002; Rephaeli et al. 2008). While the intricate nature of the astrophysical scenario lends itself to various possible explanations for the discrepancy (e.g. Carilli & Taylor 2002; Govoni & Feretti 2004), a more trivial alternative, namely that the IC estimates might be incorrect, should also be considered. There is at least one object, Coma,

where IC magnetic field measures (Fusco-Femiano et al. 1999, 2004, 2007) have been challenged (Rossetti & Molendi 2004, 2007). Moreover first measures from the *Suzaku* mission on a few objects, (i.e. A3667, Coma) are turning out to be lower limits on IC measures (Fukazawa 2007, and references therein). *XMM-Newton* measures presented in this paper seem to play a similar role in the determination of the Perseus core IC magnetic field estimates.

5.4. Future prospects

It is unlikely that either *Chandra* or *XMM-Newton* will provide significantly better estimates of the intensity of the non-thermal component in Perseus than those reported here. Clearly experiments with sensitivities extending into the hard X-ray band are the most appropriate for these kind of studies. Recently the *BAT* experiment on board the *Swift* satellite has been used to determine that an extrapolation of the non-thermal flux measured with *Chandra* to the 50–100 keV band overshoots the flux measured with *BAT* by a factor of about 4 (Ajello et al. 2008). The *Suzaku* high energy experiment (Takahashi et al. 2007), limited as it is by modest spatial resolution and by a non optimal background treatment (Kokubun et al. 2007), may provide some useful indications but will most likely not allow substantial advancement. Amongst missions that are currently under development *Simbol-X* (Ferrando et al. 2005) is arguably one of the most promising. The combination of large throughput in the 1–60 keV range, low instrumental background and *EPIC*-like spatial resolution, will allow a sensitive measurement of non-thermal components extending beyond the thermal cutoff. We have performed simulations of *Simbol-X* spectra based on our best fits for the $1'-2'$ annulus trying out different values of the normalization of the non-thermal component to determine how far down we might go. We started by taking a value of the surface brightness of 1×10^{-16} erg cm^{-2} s^{-1} arcsec^{-2}. We find that the non-thermal component dominates thermal emission above $\simeq 20$ keV and remains above background emission up to $\simeq 30$ keV. Thus, if the non-thermal emission has an intensity of this magnitude or higher it will be detected rather easily. Repeating the same exercise with a surface brightness that is ten times lower, i.e. 1×10^{-17} erg cm^{-2} s^{-1} arcsec^{-2}, we find that formal fitting of the simulated spectrum still allows a detection of the non-thermal component at the $\sim 3-4\sigma$ level, provided the observation is longer than 3×10^5 s and current estimates of the *Simbol-X* instrumental background are within 10–20% of the real value. We note that in this case the relative intensity of the non-thermal component in the 20–30 keV band is about 10%. As we have learned from the analysis of our *EPIC* data, at these intensity levels, systematics, which are at this time unknown for *Simbol-X*, will play an important, possibly dominant role. In the specific case of *Simbol-X* measurements, the critical elements which need to be kept under control at the few percent level are: the effective area calibration; the cross-calibration between the high and low energy detectors and the background. These requirements, albeit challenging, are not beyond reach, particularly if we consider that the formation flight strategy adopted by *Simbol-X* will entail some important advantages over previous missions. Extensive calibration of the telescope effective areas can be performed in flight by comparing observations of calibration sources performed with and without the telescope in the optical path. Moreover direct illumination of the *Simbol-X* focal plane, with the telescope removed, will allow an in-flight verification of the detector quantum efficiency.

Assuming that *Simbol-X* can indeed reach a sensitivity of 1×10^{-17} erg cm^{-2} s^{-1} arcsec^{-2} this will allow to detect IC components with associated B fields of roughly 1 μG, thereby providing important constraints on the magnetic field in Perseus. Given the current magnetic field estimates from Faraday rotation measures on a few cool cores (few μG: Enßlin & Vogt 2006) and the classical minimum-energy argument estimate on Perseus ($\sim 7 \mu$G: Pfrommer & Enßlin 2004), even the exquisite sensitivity within reach for *Simbol-X* might be insufficient to detect the IC emission.

6. Summary

We have carried out a detailed analysis of a long *EPIC* observation of the Perseus core in an attempt to detect and characterize a non-thermal component, our main findings may be summarized as follows:

- Systematic uncertainties play an important role in the characterization of the non-thermal component; in the absence of a strategy descending from first principles we have developed a heuristic approach to include them in our analysis.
- At variance with our preliminary estimates, we find that the non-thermal component is not detected; the surface brightness is determined to be lower than $\sim 5 \times 10^{-16}$ erg cm^{-2} s^{-1} arcsec^{-2}.
- Our *XMM-Newton* estimates are at variance with *Chandra* estimates from Sanders et al. (2005); Sanders & Fabian (2007) and from our own analysis; the most likely explanation for the discrepancy between *Chandra* and *XMM-Newton* is a problem in the *Chandra* effective area calibration.
- Our *EPIC* based upper-limit on the surface brightness converts into IC magnetic field lower limits of $\sim 0.4 \mu$G for the $0.5'-1'$ annulus and $\sim 0.3 \mu$G for the $1'-2'$ annulus; these measures are not in disagreement with RM estimates on a few cool cores (few μG: Enßlin & Vogt 2006) and the minimum energy estimate on Perseus (10 μG: Pfrommer & Enßlin 2004).
- In the not too distant future *Simbol-X* may allow detection of non-thermal components with intensities more than 10 times lower than those that can be measured with *EPIC*; nonetheless even the exquisite sensitivity within reach for *Simbol-X* might be insufficient to detect the IC emission from Perseus.

References

Ajello, M., Rebusco, P., Cappelluti, N., et al. 2008, ApJ, submitted
Anders, E., & Grevesse, N. 1989, Geochim. Cosmochim. Acta, 53, 197
Carilli, C. L., & Taylor, G. B. 2002, ARA&A, 40, 319
Cassano, R., Brunetti, G., Setti, G., Govoni, F., & Dolag, K. 2007, MNRAS, 378, 1565
Clarke, T. E. 2004, J. Korean Astron. Soc., 37, 337
David, L. P., Nevalainen, J., & Bonamente, M. a. 2007, in Proceedings of the 2007 Chandra Calibration Workshop
De Grandi, S., & Molendi, S. 2008, in preparation
Drake, J. J., Ratzlaff, P., Kashyap, V., et al. 2007, Chandra News, 14, 47
Ehle, M., Breitfellner, M., Gonzales Riestra, R., et al. 2007, XMM-Newton Users' Handbook, http://xmm.esac.esa.int/external/xmm_user_support/documentation/uhb_2.5/index.html
Enßlin, T. A., & Vogt, C. 2003, A&A, 401, 835

Enßlin, T. A., & Vogt, C. 2006, A&A, 453, 447

Fabian, A. C., Sanders, J. S., Taylor, G. B., et al. 2006, MNRAS, 366, 417

Ferrando, P., Goldwurm, A., Laurent, P., et al. 2005, in Optics for EUV, X-Ray, and Gamma-Ray Astronomy II, presented at the Society of Photo-Optical Instrumentation Engineers (SPIE) Conference, ed. O. Citterio, & S. L. O'Dell, Proc. SPIE, 5900, 195

Fukazawa, Y. 2007, in The Suzaku X-ray Universe, http://heasarc.nasa.gov/docs/suzaku/sandiego2007/dec11/fukazawa.pdf

Fusco-Femiano, R., dal Fiume, D., Feretti, L., et al. 1999, ApJ, 513, L21

Fusco-Femiano, R., Orlandini, M., Brunetti, G., et al. 2004, ApJ, 602, L73

Fusco-Femiano, R., Landi, R., & Orlandini, M. 2007, ApJ, 654, L9

Govoni, F., & Feretti, L. 2004, Int. J. Mod. Phys. D, 13, 1549

Grupe, D. 2001, ArXiv Astrophysics e-prints

Huchra, J. P., Vogeley, M. S., & Geller, M. J. 1999, ApJS, 121, 287

Jerius, D., Marshall, H. L., & David, L. P. 2008, in EPIC Calibration workshop, 79

Kirsch, M., & EPIC-Consortium 2007, EPIC status of calibration and data analysis, http://xmm.esac.esa.int/docs/documents/CAL-TN-0018.pdf

Kokubun, M., Makishima, K., Takahashi, T., et al. 2007, PASJ, 59, 53

Leccardi, A., & Molendi, S. 2007, A&A, 472, 21

Leccardi, A., & Molendi, S. 2008, in press

Molendi, S., & Sembay, S. 2003, Assesing the EPIC spectral calibration in the hard band with a 2C273 observation, http://xmm.vilspa.esa.es/docs/documents/CAL-TN-0036-1-0.ps.gz

Pfrommer, C., & Enßlin, T. A. 2004, MNRAS, 352, 76

Rephaeli, Y., Gruber, D. E., & Rothschild, R. E. 1987, ApJ, 320, 139

Rephaeli, Y., Nevalainen, J., Ohashi, T., & Bykov, A. M. 2008, Space Sci. Rev., 134, 71

Rossetti, M., & Molendi, S. 2004, A&A, 414, L41

Rossetti, M., & Molendi, S. 2007, ArXiv Astrophysics e-prints

Rudnick, L., & Blundell, K. M. 2003, ApJ, 588, 143

Sanders, J. S., & Fabian, A. C. 2007, MNRAS, 381, 1381

Sanders, J. S., Fabian, A. C., Allen, S. W., & Schmidt, R. W. 2004, MNRAS, 349, 952

Sanders, J. S., Fabian, A. C., & Dunn, R. J. H. 2005, MNRAS, 360, 133

Stuhlinger, M., Kirsch, M. G. F., Santos-Leo, M., et al. 2008, Status of the XMM-Newton instrument cross-calibration with SASv7.1, http://xmm.esac.esa.int/docs/documents/CAL-TN-0052-5-0.ps.gz

Takahashi, T., Abe, K., Endo, M., et al. 2007, PASJ, 59, 35

Taylor, G. B., Fabian, A. C., & Allen, S. W. 2002, MNRAS, 334, 769

Taylor, G. B., Gugliucci, N. E., Fabian, A. C., et al. 2006, MNRAS, 368, 1500

Vogt, C., & Enßlin, T. A. 2005, A&A, 434, 67